Cloud and Precipitation Particle Identification Using Cloud Radar and Lidar Measurements: Retrieval Technique and Validation

Ulrike Romatschke[1] and Jothiram Vivekanandan[1]

[1]Earth Observing Laboratory, National Center for Atmospheric Research (NCAR), Boulder, CO 80301, USA.

Corresponding author: Ulrike Romatschke (romatsch@ucar.edu)

Key Points:

- A fuzzy logic hydrometeor particle identification method is presented that uses airborne cloud radar and lidar observations.
- A comparison of hydrometeor classifications with independent in-situ measurements of Southern Ocean clouds show agreement in over 70% of cases.

Abstract

This paper describes a technique for identifying hydrometeor particle types using airborne HIAPER Cloud Radar (HCR) and High Spectral Resolution Lidar (HSRL) observations. HCR operates at a frequency of 94 GHz (3 mm wavelength), while HSRL is an eye-safe lidar system operating at a wavelength of 532 nm. Both instruments are deployed on the NSF-NCAR HIAPER aircraft. HCR is designed to fly in an underwing pod and HSRL is situated in the cabin. The HCR and HSRL data used in this study were collected during the Southern Ocean Clouds, Radiation, Aerosol Transport Experimental Study (SOCRATES). Comprehensive observations of the vertical distributions of liquid and mixed-phase clouds were obtained using in-situ probes on the aircraft and remote sensing instruments. Hydrometeor particle types were retrieved from HCR, HSRL, and temperature fields with a newly-developed fuzzy logic particle identification (PID) algorithm. The PID results were validated with in-situ measurements collected onboard the HIAPER aircraft by a 2D-Stereo (2D-S) cloud probe. Particle phases derived from the PID results compare well with those obtained from the 2D-S observations and agree in over 70 % of cases. Size distributions are also consistent between the two methods of observation. Knowledge of the particle type distribution gained from the PID results can be used to constrain microphysical parameterizations and improve the representation of cloud radiative effects in weather and climate models.

1 Introduction

The knowledge of cloud and precipitation particle types, that is, their phase and size distribution, aids our understanding of cloud microphysical and dynamic processes, and their representation in weather and climate models. A multitude of cloud microphysics parametrization schemes are used in weather and climate models, such as bulk microphysics schemes, which describe bulk properties of clouds within a grid volume (Thompson et al., 2008; Tao & Simpson, 1993: Morrison et al., 2008; Lin & Colle, 2011, Paukert et al., 2019), bin microphysics schemes, which represent particle distributions explicitly (Khain et al., 2004; Khain et al., 2010), and Lagrangian schemes, which represent particle populations by a discrete sampling of cloud and precipitation particles (Morrison et al., 2020).

Liquid and frozen particles in clouds play a crucial role in the earth's radiation budget by scattering shortwave radiation and absorbing and re-emitting longwave radiation. However, the

radiative properties of liquid and frozen particles are not the same, and clouds with higher fractions of supercooled liquid are generally optically thicker, and reflect more solar radiation back to space (Sun & Shine, 1994; Bjordal et al., 2020). Accurate representation of the base state of cloud phase in cloud microphysics parameterization schemes is therefore crucial for the prediction of cloud and earth radiation budgets, and ultimately the climate feedback of clouds (Tan et al., 2016; Zelinka et al., 2020). Identification of particle phase is especially important for stratocumulus clouds as they are a dominant cloud type, covering large regions of the globe (Wood, 2012).

It has been shown that the amount of supercooled liquid in clouds is often underestimated in models compared to observations (Komurcu et al., 2014). One reason for this discrepancy is that the growth of ice crystals at the expense of surrounding supercooled liquid droplets in a mixed-phase cloud, i.e., the Wegener-Bergeron-Findeisen process (Wallace & Hobbs, 2006), becomes too efficient in theoretical applications. In a self-contained air parcel with liquid and ice particles, and in the absence of any external dynamical forcing, theoretical studies suggest that the glaciation time scale is on the order of an hour (Korolev & Isaac, 2003). However, observational studies indicate that supercooled liquid droplets and frozen particles can continue to exist in individual layers or in mixed-phase conditions for much longer periods, even days (de Boer et al., 2011). Specifically, observations of mixed-phase stratocumulus clouds in mid-latitude and polar regions show a thin liquid layer at the cloud top, while cloud droplets, drizzle, and frozen particles coexist within the cloud (de Boer et al., 2011).

Another of the suggested reasons for the underestimate of cloud liquid in models is, that mixed-phase clouds are poorly constrained because of the difficulty of obtaining observations (Tan et al., 2016). Satellite observations have proven valuable for constraining cloud radiative effects in models (Tan et al., 2016; McCoy et al., 2014), but they are restricted to observing cloud tops only. In-situ measurements are considered the best means for observing microphysical properties of clouds and precipitation particles, but they are often limited in spatial and temporal extent. Remote sensing instruments are well suited to expand hydrometeor observations spatially and temporally. For example, cloud radar and lidar measurements were used to retrieve the effective radius of droplets and the liquid water content in stratiform precipitation in regions away from the aircraft track, where in-situ measurements could not be obtained (Vivekanandan et al., 2020). The Cloudnet project established several sites with different types of remote

sensors, to collect long-term cloud microphysics observations for model evaluation and improvement (Illingworth et al., 2007). However, since remote sensing instruments do not provide direct measurements of particle phase, type, and size, retrieval algorithms are necessary for the microphysical characterization of particles. Individual remote sensing fields, such as reflectivity alone, cannot be used to discriminate between liquid and ice, as there is a significant overlap in observed reflectivity values between liquid and frozen precipitation (Section 3.2). The combination of measurements from remote sensing instruments operating at different wavelengths reduces ambiguity in differentiating liquid from frozen particles.

Many techniques for identifying hydrometeor particles in remote sensing observations from multiple instruments and wavelengths exist. Many use thresholds or rigid boundaries and identify particles in a decision-tree manner. Shupe (2007) apply thresholds to ground-based radar and lidar measurements of Arctic clouds to identify different particle types in case studies. Decision-tree and rigid boundary techniques were also applied to spaceborne CloudSat and CALIPSO observations (Ceccaldi et al, 2013; Kikuchi et al., 2017). Thresholds on particle fall speed, derived from Doppler velocity measurements from vertically pointing radars, have recently been integrated into decision-tree hydrometeor classification algorithms (Sokol et al., 2020; Garcia-Benadi et al., 2020). Because of the aforementioned overlap in remote measurements for different particle types, rigid boundaries can misclassify particle types.

Machine learning techniques can also be used for classifying hydrometeor types. Neural networks in particular have been used for particle characterization (Liu and Chandrasekar, 2000), or detection of supercooled liquid (Luke et al., 2010) or riming (Vogl et al., 2022) in mixed-phase clouds. Roberto et al. (2017) used a Support Vector Machine (SVM) to classify particles in dual-polarization radar observations, which was trained and evaluated with classifications from a fuzzy-logic algorithm. Recent applications of machine learning techniques also include the detection and classification of biological scatterers (Chilson et al., 2019; Jatau et al., 2021) and pyrometeors (McCarthy et al., 2020) in radar observations.

Fuzzy-logic methodologies are well suited for classifying hydrometeors with overlapping and smooth transition boundaries in clouds and precipitation. They have been extensively used for ground based applications (Vivekanandan et al., 1999; Zrnić et al., 2001, Liu &

Chandrasekar, 2000; Lim et al., 2005; Dolan & Rutledge, 2009), and are applied to ground-based radar network observations on a routine basis (Park et al., 2009).

A challenge faced by many of these methods is a lack of direct observations of particle types, which can be used for verification of the derived particle types, or – in case of neural networks – for training purposes. Some of the existing algorithms are therefore not validated at all (e.g. Shupe et al., 2007), while others are validated using proxies such as Ceilometer, microwave radiometer, and radiosonde measurements (e.g. Luke et al., 2010). Comparisons to other particle identification algorithms are another means of validating results (e.g. Kalesse-Los et al., 2022).

This paper describes a fuzzy logic methodology for identifying cloud and precipitation particle types developed for airborne cloud radar and lidar observations. To our knowledge, it is the first fuzzy logic particle identification algorithm for airborne measurements. It was developed and validated using measurements from the Southern Ocean Clouds, Radiation, Aerosol Transport Experimental Study (SOCRATES) field campaign. The use of SOCRATES datasets, which include co-located remote sensing and in-situ observations, provides the opportunity to validate the algorithm with direct observations of particle type, phase, and size. Section 2 describes the SOCRATES field campaign and the remote sensing and in-situ instruments and corresponding datasets. Section 3 describes the basic components of the PID algorithm and the fuzzy logic method. Information on how the algorithm was tuned and validated with in-situ observations are presented in Section 4. Conclusions are drawn in Section 5.

2 Description of instruments and datasets

2.1 SOCRATES

As part of its mission to aid the scientific community in observational field campaigns, the Earth Observing Laboratory (EOL) at the National Center for Atmospheric Research (NCAR) deploys the High-performance Instrumented Airborne Platform for Environmental Research (HIAPER), a Gulfstream V research aircraft. The PID method described in this study was developed using data collected during the SOCRATES field campaign, where remote sensing and in-situ instruments were deployed on HAIPER (McFarquhar et al., 2020).

136 During SOCRATES, the aircraft flew 15 research flights (RFs) consisting of north-south
137 transects south of Hobart, Australia, between 15 January and 24 February, 2018. The
138 SOCRATES flight plans were designed to collect datasets which would enable characterization
139 of the free troposphere and boundary layer over the Southern Ocean as a function of latitude
140 (McFarquhar et al., 2020). Flight plans were adjusted in the field to target Marine boundary layer
141 clouds in the cold sectors of cyclones. Flights consisted of higher altitude (~6 km) ferry legs to
142 and from the target area at the beginning and end of the flights, where the remote sensing
143 instruments were mostly operated in nadir pointing mode. At the target area, the aircraft
144 descended to lower altitudes where in-cloud maneuvers were performed. During these
145 maneuvers the aircraft switched between flying a few hundred meters below cloud base and
146 above cloud top, with frequent cloud crossings in between. The remote sensing instruments
147 changed pointing direction accordingly, from zenith during below-cloud segments to nadir in
148 above-cloud segments. Flights operated during local daytime from ~21:00 UTC to 8:30 UTC.

149 2.2 Remote sensing instruments

150 Two of the instruments requestable by the scientific community as part of the HIAPER
151 instrument suite are the HIAPER Cloud Radar (HCR, Vivekanandan et al., 2015) and the
152 Gulfstream V High Spectral Resolution Lidar (HSRL). HCR is a dual-polarimetric millimeter-
153 wavelength W-band radar that is deployed in an underwing pod on HIAPER. It has collected
154 data in four major and one minor field campaigns, ranging in location from the Southern Ocean
155 to the tropics (Albrecht et al., 2019; Fuchs-Stone et al., 2020; McFarquhar et al., 2020; Rauber et
156 al., 2017). Care has been taken to optimize radar calibration and data quality, and provide
157 additional data products, such as reanalysis fields or melting layer altitude (Ellis et al., 2019;
158 Romatschke, 2021; Romatschke et al., 2021; Romatschke & Dixon, 2022). HCR observations
159 are computed with a resolution of ~20 m in range and a temporal resolution of 10 Hz. The along-
160 track spatial resolution is a function of aircraft speed and the dwell time of the sample. At typical
161 flight speeds of 200 ms^{-1}, the 10 Hz temporal resolution yields a sample volume of
162 approximately 20 m in the direction of flight. The HCR beam's footprint is 3 m at a range of 250
163 m and it increases to 180 m at 15 km in range. Polarimetric and Doppler radar fields are
164 calculated from the measured in-phase and quadrature (I/Q) time-series data. The dynamic range
165 of the HCR reflectivity is between -35 and +30 dBZ and can be estimated with a 1-2 dB accuracy
166 (Romatschke et al., 2021).

The HSRL is a calibrated lidar (Razenkov et al., 2008) and operates at a wavelength of 532 nm with a pulse repetition frequency of 4000 Hz and average power of 300 mW. It uses a high-repetition, low-pulse energy laser which meets the eye-safety criteria of the American National Standards Institute (ANSI) at all ranges. It samples the atmosphere with a temporal resolution of 2 Hz and a range resolution of 7.5 m. HSRL measures the backscatter coefficient and depolarization properties of atmospheric aerosols and clouds, and the cloud extinction coefficient.

For the purposes of this study, HCR and HSRL data were resampled onto a common grid. The HCR data was averaged to 2 Hz to match HSRL's temporal resolution. Then in the vertical the HSRL range gate closest to each HCR gate was used to re-sample the 7.5 m HSRL data onto the 19 m HCR range resolution. Both instruments are capable of operating in nadir and zenith pointing modes. HCR has a rotatable reflector which allows for 240° cross-track scanning and the antenna is stabilized when staring in nadir or zenith directions. HSRL can be manually turned to point either nadir or zenith through specially designed windows in the aircraft floor and ceiling. (HSRL points 4 degrees off zenith and nadir to avoid specular reflection from horizontally-oriented ice particles.) During SOCRATES the radar and lidar operator intended to point both instruments in the same direction at all times but since the manual rotation of HSRL takes about half a minute, some discrepancies in the pointing direction were unavoidable. The datasets were merged only when the two instruments were pointing in the same direction, within some margin of pointing error. Also, since the HSRL pointing angle is fixed relative to the aircraft, it pointed off zenith/nadir during aircraft turns. Therefore, during aircraft turns the data sets were not merged and the HSRL data were set to missing.

The radar fields that were used in the HCR-HSRL combined PID algorithm development are reflectivity (DBZ), radial velocity (VEL), and linear depolarization ratio (LDR). In earlier versions of the PID algorithm, the HCR Doppler spectrum width field was also included but we found that it did not provide additional value. It was therefore eliminated to simplify the algorithm. The lidar variables were the aerosol backscatter coefficient (BACKSCAT) and the lidar linear depolarization ratio (LLDR). The altitude of the lowest melting layer at each time step was utilized in post-processing (Romatschke, 2021). Note that we differentiate between the freezing level of 0 °C and the melting layer where actual melting occurs. Outside of regions with significant updrafts, the melting layer is generally located below the freezing level of 0 °C

(Romatschke, 2021). In addition, ERA5 temperatures (TEMP, European Centre for Medium-Range Weather Forecasts, 2018) interpolated to the HCR-HSRL time-range grid (Romatschke et al., 2021) were used. Note that measurements from dropsondes launched from HIAPER during SOCRATES were assimilated into ERA5 which resulted in a highly accurate temperature reanalysis field (Romatschke, 2021).

A trimmed-down version of the PID algorithm can be applied to the HCR radar fields alone (Section 3.4) to provide particle information for field campaigns where HSRL was not deployed. This HCR stand-alone algorithm was created using the 10 Hz HCR data.

The proposed PID method was applied to data from all HCR-HSRL combined and HCR-only field campaigns. All data is available in the EOL Field Data Archive (NCAR/EOL HCR Team, 2022a, 2022b, 2022c, 2022d; NCAR/EOL HCR Team & NCAR/EOL HSRL Team, 2022a, 2022b).

2.3 2D cloud probes

To tune the PID scheme and validate the results (Section 4) we used the University of Washington Ice-Liquid Discriminator (UWILD) particle phase classifications and size distributions. They are based on 2-Dimensional Stereo (2D-S) cloud probe (Lawson et al., 2006) measurements. The 2D-S cloud probe was deployed on HIAPER during SOCRATES and imaged particles with diameters ranging from 0.01 to 1.28 mm. The UWILD dataset is available in the EOL Field Data Archive (Atlas et al., 2021; Mohrmann et al., 2021) for RF01 to RF14 - no cloud probe data was collected in RF15 and RF15 was therefore not used in this study.

UWILD uses 14 parameters computed from binary 2D-S images in a random forest algorithm, to predict the liquid or frozen phase of particles observed in the images (Atlas et al., 2021). The algorithm has an accuracy of 95%, and the phase of all detected particles, which is provided in different size bins at a 1 Hz resolution, is therefore an excellent dataset to compare to the particle phases and sizes derived with the PID scheme. One of the limitations of the UWILD dataset is that it only provides phase classifications for particles with diameters larger than 0.056 mm. It is further limited by data quality issues of the 2D-S images, which include out-of-focus images, and large particles being truncated at the edge of the image buffer. UWILD also has a slight bias towards misclassifying large liquid particles as ice (Atlas et al., 2021).

3 The PID algorithm: basic principle

In this section the basic principle of the PID algorithm is described. The method and input parameters were developed and adjusted on a subset of the data during a tuning process, which is described in detail in Section 4. The PID algorithm consists of three basic data processing steps. In the pre-processing step, we determine which subsets of the radar and lidar fields can be used for specific purposes, and mask unsuitable data. The second step applies a fuzzy logic scheme to identify the particle types. In the post-processing step, minor adjustments are made to the particle classification based on a priori knowledge.

3.1 Pre-processing

The PID technique retrieves particle size and particle phase (liquid and frozen). Variables suitable for size characterization are DBZ and VEL (which we will call the size-defining fields). LDR and LLDR (the phase-defining fields) are used to distinguish between liquid and frozen particles. The TEMP field only provides a weak indication of particle phase as liquid particles can be observed well below the freezing point (Houze, 2014). BACKSCAT offers a limited capability for detecting particle phase, but it is not reliable by itself. Therefore it is only used in regions where LLDR is also present.

In the warm regions below the melting layer, only liquid particles are expected to be present. We therefore do not use the phase defining fields LDR, LLDR, and BACKSCAT below the melting layer. TEMP is retained to constrain the melting particles (Section 3.2) to within a certain distance of the melting layer. The remaining fields, DBZ and VEL, discriminate between the different particle sizes in the warm regions.

Particle phase discrimination is most challenging above the melting layer because both, supercooled liquid and frozen particles, can exist at temperatures well below freezing. We rely on the major phase-defining fields LDR and LLDR to distinguish liquid from frozen particles. However, these fields exist only where the weak cross-pol signal is above the noise floor. As DBZ and VEL are unsuitable for phase discrimination, and TEMP alone does not fulfill the purpose, no attempt is made to determine particle phase in regions where neither of the phase-defining fields is usable. TEMP is unused in these areas as it does not benefit size estimation.

It is important to note that the Doppler velocity is the sum of the particle fall speed and the air motion. Ideally, particle size is inferred from particle fall speed alone, without the air

motion component, and it is therefore not appropriate to use VEL in areas of significant air motion. To find such areas a velocity texture field is used (Romatschke & Dixon, 2022). The texture field is a measure of the smoothness of the VEL field on the horizontal dimension. VEL is not used in areas with high velocity texture values above the melting layer.

3.2 Fuzzy logic scheme

Fuzzy logic is a powerful tool for classifying hydrometeors in HCR and HSRL field measurements. Its biggest strength is that it combines a range of input fields instead of relying on fixed thresholding of values from individual fields. It also allows for smooth transitions between various cloud and precipitation particle type classifications.

The core components of a fuzzy logic method are the membership functions (MFs). The MFs describe how likely a specific value of a measured input field is a member of the desired output hydrometeor classification on a scale of 0 (no member) to 1 (member). Since the values of the MFs vary between 0 and 1, they can more realistically represent the degree to which a particular measurement identifies a specific hydrometeor type. Initial shapes of the MFs were determined using information from previous studies (Houze, 2014; Shupe, 2007). The final MFs were determined during the tuning process described in Section 4 and are shown in Figure 1.

The six input fields for the fuzzy logic scheme are DBZ, VEL, LDR, LLDR, BACKSCAT, and TEMP (Section 2.2) which were initially mapped to six output fields: three liquid categories with decreasing drop sizes (rain, drizzle, cloud drops), two frozen categories (large frozen, small frozen), and one category representing melting particles (melting).

The MFs of the size-defining fields were chosen to represent the particle types from small to large. The small classes (cloud drops, small frozen) are most likely in the low DBZ regions, while increasing reflectivity suggests drizzle and ultimately raindrop-sized and large frozen particles (Figure 1a). Melting particles can occur at all reflectivity values. VEL MFs roughly follow fall speeds described in (Houze, 2014) which were adjusted to match to the corresponding DBZ categories during the tuning process (Figure 1b).

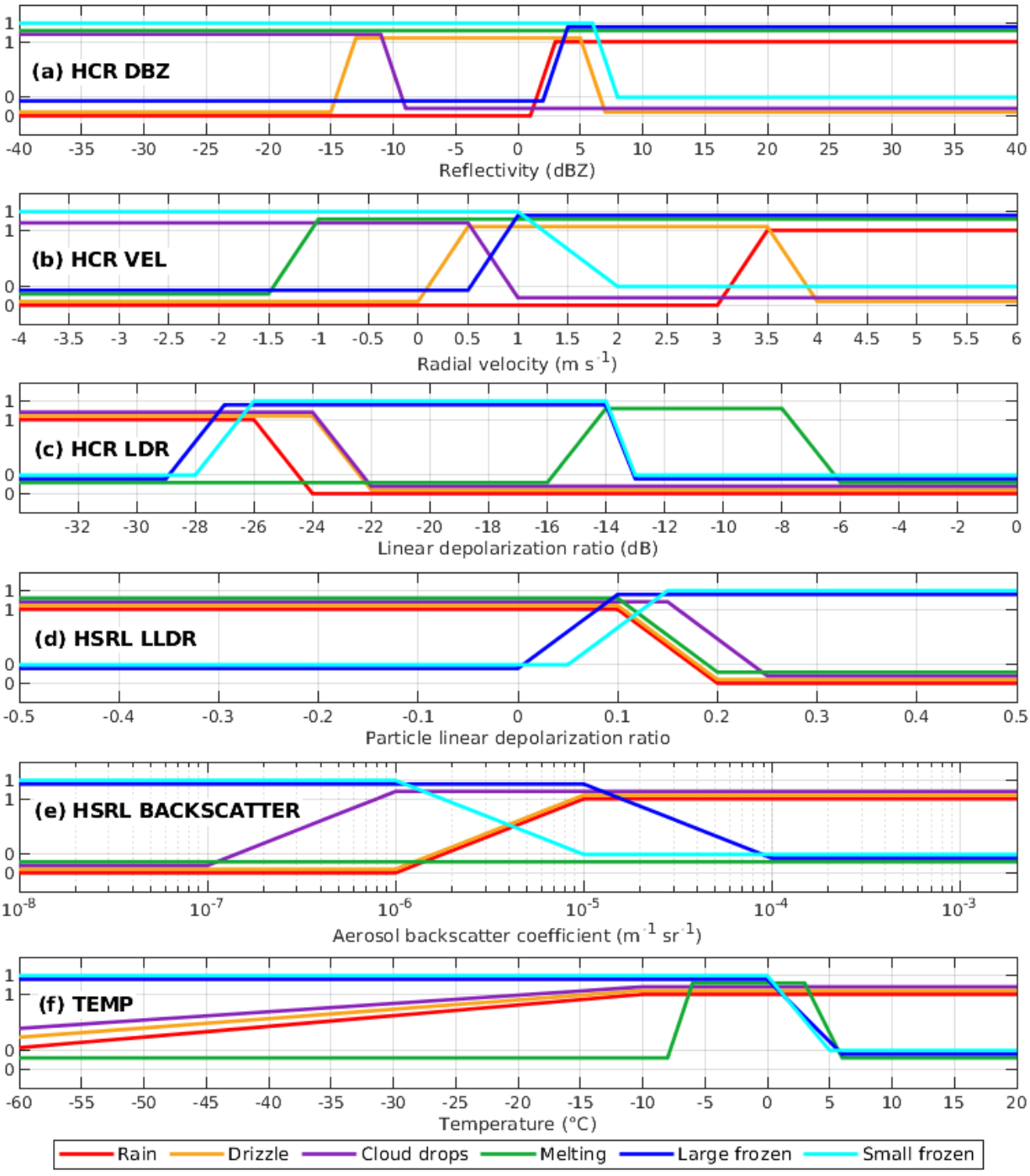

283

284 **Figure 1**. Membership functions for the six input fields (top to bottom) and six initial
285 hydrometeor types (colored lines).

286 The MFs of LDR and LLDR are low for axisymmetric particles such as liquid drops, but
287 high for irregularly shaped ice particles in zenith and nadir pointing (Figure 1c and d). In other
288 words LDR and LLDR are higher in areas with frozen particles due to their non-spherical shape.
289 BACKSCAT is higher in high concentrations of small liquid drops than in small concentrations

of ice-dominated regions (Figure 1e, Shupe, 2007). Interestingly, during the tuning process we found that the phase change from liquid to ice occurs at higher LLDR values for small particles than for large ones. For BACKSCAT, the ice to liquid transition occurs at smaller values for large than for small particles. The highest LDR values are associated with melting particles, mostly in the bright band region (Romatschke, 2021).

As already mentioned, TEMP is only a mild indicator of particle phase in cold regions. Nonetheless, the likelihood of liquid drops still somewhat decreases with decreasing temperature (Figure 1f). The MFs of the liquid categories for TEMP were set relatively high, even for temperatures well below freezing. High MF values imply that liquid classifications are almost as likely as frozen classifications. It is therefore unlikely that TEMP becomes the deciding factor for the distinction between liquid and frozen particles, and the algorithm will decide particle phase based on the more reliable phase defining fields.

Melting particles are unlikely to occur at extremely low temperatures. In regions of above 0 °C temperatures, frozen particles are unlikely to occur. However, as it was observed that there can be a significant vertical distance between the freezing level and the melting layer (Romatschke, 2021), we phase out frozen and melting particles from 0 °C to 5 °C.

Once the shapes of the MFs were determined, they were used to map the input fields to the so-called fuzzy fields where each input value is then represented by a value between 0 and 1. This step created 36 fuzzy fields (P_i^j), from the six particle types (i) and six input fields (j). Each fuzzy field was then multiplied with a predetermined weight (W_j) which represents the robustness of the respective input field for determining particle phase or size and the measurement accuracy of the input field. The weights were adjusted during the tuning phase and set to 22% for DBZ, 16% for VEL, 16% for LDR, 16% for LLDR, 14% for BACKSCAT, and 16% for TEMP. The weighted fuzzy fields ($P_i^j W_j$) were summed to produce a single aggregated field (Q_i) for each of the six particle types:

$$Q_i = \sum_{j=1}^{6} P_i^j W_j. \quad (1)$$

The aggregated field with the maximum value was identified as the likely particle type for the given observations.

317 The mathematical operations involved in the above-described fuzzy logic procedure are
318 (a) mapping of the input variables to the fuzzy fields, (b) multiplication of the fuzzy fields with
319 the weights and aggregation, and (c) finding the maximum among the aggregated values for
320 particle-type identification. The simplicity and efficiency of the method is suitable for real-time
321 classification and display of hydrometeor types.

322 ### 3.3 Post-processing

323 In the first post-processing step, classifications of particles above the melting layer where
324 neither LDR nor LLDR is present were reassigned in the following way: Particles identified as
325 cloud liquid and small frozen were grouped in a new small particle category (cloud), and drizzle,
326 rain, melting, and large frozen particles were classified as an additional large particle category
327 (precipitation). This step is necessary because a phase assessment without the phase defining
328 fields is ambiguous. However, there is one exception to this rule. As described in Section 4.3,
329 regions with very low DBZ values are dominated by liquid phase particles. Therefore particles in
330 regions with no phase defining fields, but DBZ≤-30 dBZ were identified as cloud liquid.

331 In the next step, the liquid particles above the freezing level were identified and labeled
332 as supercooled (SC). Hence, the eleven final particle classes are rain, SC rain, drizzle, SC
333 drizzle, cloud liquid, SC cloud liquid, melting, large frozen, small frozen, cloud, and
334 precipitation.

335 In the warm region below the melting layer we do not allow frozen particle types, or
336 melting particles in regions with no LDR and no LLDR. Grid points fulfilling these criteria were
337 replaced with the nearest neighboring particles of the non-frozen categories. Only a small
338 number of particles were re-classified in this post-processing step.

339 One last post-processing step was necessary because HCR samples the first valid data at
340 range gate 18 at a range of 107 m off the aircraft, while HSRL starts sampling at range gate 21
341 (165 m). To avoid unrealistic category borders at gate 21, we checked whether the first three
342 valid HCR gates (18, 19, and 20) were assigned the same category, but a different category from
343 the first HSRL range gate 21. If that was the case, we removed the phase classification from the
344 first three valid HCR range gates and replace them with the cloud or precipitation categories.
345 More trust was put into the range gate with both HCR and HSRL measurements since our
346 analysis (Section 4.2) showed that PID from combined measurements is likely more accurate.

3.4 HCR stand-alone algorithm

To identify particle types for field campaigns where HCR was deployed, but HSRL was not, we created a version of the PID algorithm that uses only HCR data. The principle of the algorithm is the same as for the HCR-HSRL combined algorithm. It was based on the same membership functions but only for the DBZ, VEL, LDR, and TEMP input fields. The weights in the fuzzy logic scheme were set to 34% for DBZ and 22% for the other three fields. The HCR stand-alone algorithm relies on LDR as the sole phase defining field. Therefore, regions where LDR was not valid were classified as cloud or precipitation, except for regions of DBZ≤-30 dBZ, which were set to cloud liquid (Section 4.3). The limited coverage of LDR lead to a significantly reduced number of pixels with phase classification.

4 Algorithm tuning and validation

4.1 Tuning process

To tune the HCR-HSRL combined, and HCR stand-alone algorithms with a tuning dataset, and assess their performance with a validation dataset, PID classifications were visually and quantitatively compared with the 1 Hz aggregated product from the UWILD in-situ cloud probe algorithm (Section 2.3). UWILD separates all particles, time-stamped within one second, into liquid and ice phase, and then sorts them into 50 logarithmically spaced size bins.

To tune and validate the MFs of the PID algorithm, the cases and times when coincident remote sensing and UWILD data were available, were roughly divided in half, into a tuning and a validation dataset. For the tuning dataset, 27 representative cases observed throughout the field campaign were selected. We chose manual selection over an automatic approach to ensure that the cases covered all types of clouds and conditions observed during SOCRATES in both the tuning and the validation dataset. The tuning cases came from ten different research flights and were distributed over all SOCTATES latitudes. Their duration ranged from a few minutes to over 20 minutes and they were sampled at times ranging from 21:30 UTC to 05:30 UTC.

The PID algorithm with the initial MFs derived from the literature (Section 3.2) was applied to the tuning dataset. The PID results from this initial application were visually and statistically compared to UWILD data as described in the following Section 4.2. The MFs and weights were then carefully adjusted to improve the accuracy of the PID algorithm in an iterative process until no further improvement could be achieved. The algorithm with the final MFs was

then applied to the validation dataset. The statistical results computed from the application on the validation dataset were used to assess the accuracy of the algorithm as described in Sections 4.2 and 4.6. We chose manual tuning of the MFs over the use of an analytical optimization tool since it can take a vertical offset of 100-200 m between the cloud probe and the first valid HCR and HSRL range gates into account (see Sections 4.1 and 4.4 for details on this offset and how it can affect the comparison). Manual tuning also allowed adjustments for known problems in the cloud probe dataset (Section 2.3).

4.2 Hydrometeor phase

In the first part of the tuning and validation, we focus on the phases detected by the PID scheme and compare them to the phases provided by UWILD. It is important to note that HCR measurements are dominated by the largest particles present in a sampling volume in the Rayleigh scattering regime. For a W-band radar, particles up to a diameter of 0.3 mm are in the Rayleigh region while particles larger than 0.3 mm are in the Mie region (Ellis & Vivekanandan, 2011; Zhang, 2019). For example, a few large snowflakes in a volume that is otherwise dominated by a large concentration of small liquid drops will result in a classification of large frozen, as return power is proportional to the 6^{th} power of the particle sizes. HSRL variables are not dominated by the largest particles. However, in the combined algorithm the HCR input fields were assigned combined weights of 54% whereas the HSRL variables were assigned 30% (Section 3.2). The results are therefore dominated by the HCR variables and to compare UWILD data with PID results, the analysis focuses on the largest particles detected by UWILD. In the 1 Hz aggregated UWILD product, from the large end of the size bin spectrum, the total number of particles in each size bin were cumulatively added until a minimum of 20 particles was reached. (Varying the minimum number of particles between 10 and 40 changed the results by up to 4%.) We call the aggregated size bins with these largest particles the *UWILD bucket*. We then calculated the liquid fraction for the UWILD bucket by dividing the number of liquid particles by the total number of particles in the UWILD bucket at each 1 s time step (similar to the liquid fraction used by Atlas et al., 2021). The average size of the UWILD bucket was recorded and used for size validation (Section 4.6). Since HSRL measurements are not sensitive to the largest particles, all UWILD particles were used to calculate statistics for the LLDR regions (see below).

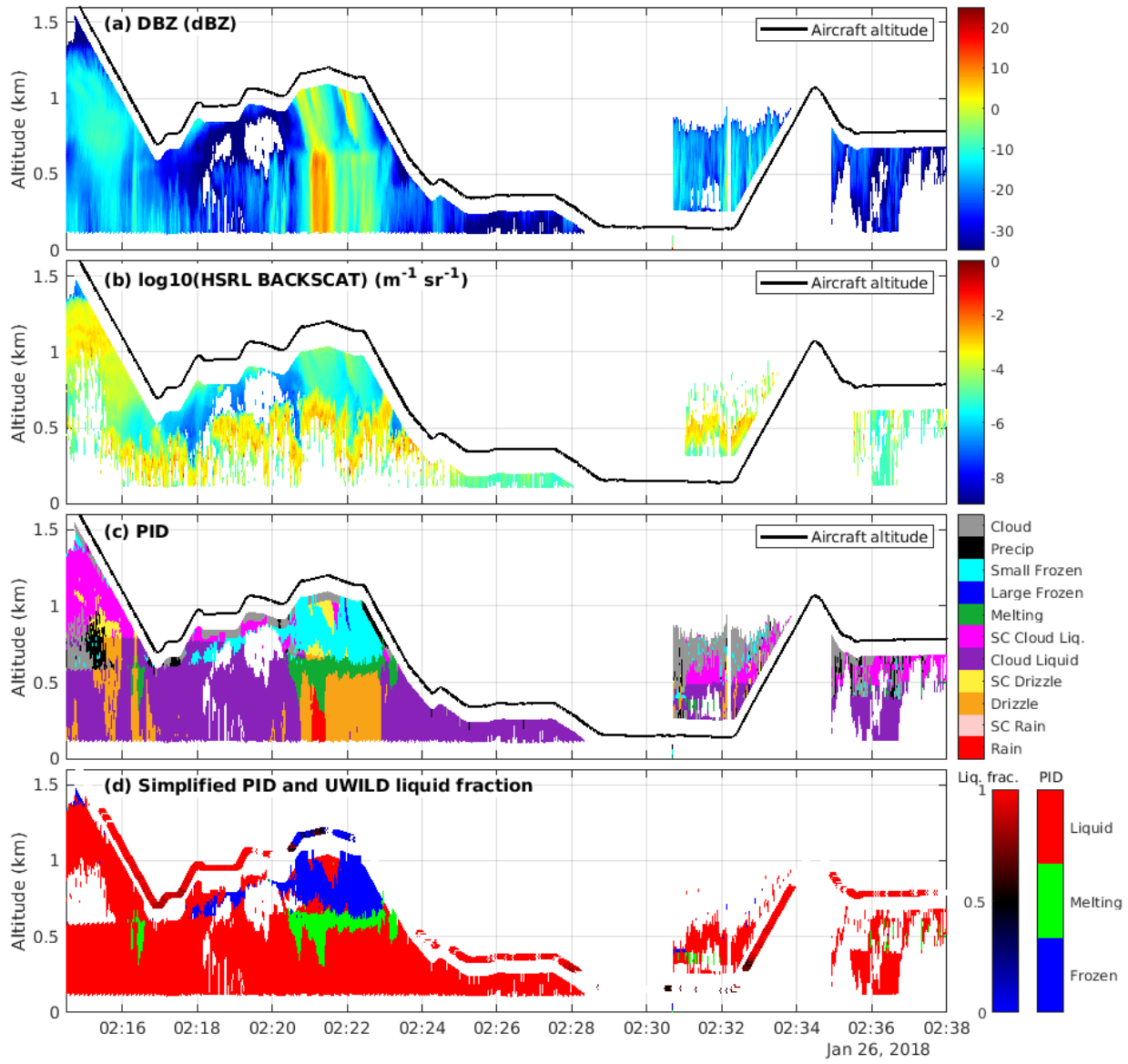

Figure 2. (a) HCR DBZ and (b) HSRL BACKSCAT (c) PID (color shading) and aircraft altitude (black line). (d) Simplified PID (color shading) and UWILD liquid fraction (colored line at aircraft altitude).

The UWILD liquid fraction was visually compared to the PID categories during the tuning phase. To aid this comparison, we simplified to only three PID categories, frozen, liquid, and melting, by combining the different liquid and frozen categories accordingly. The simplified PID categories were plotted and the UWILD liquid fraction was added to the plots as a line at flight altitude. All SOCRATES data was plotted after the final tuning, to detect strengths and weaknesses of both datasets. The main conclusions drawn from this visual comparison of PID

and UWILD phase detections are illustrated in an example (Figure 2), which shows both nadir and zenith pointing data collected on January 26, 2018, from 02:14 to 02:38 UTC.

Overall the comparison shows good agreement between the UWILD and the PID phases. UWILD liquid fractions tend to be high where the PID scheme detects liquid particles and low in areas of frozen particles (Figure 2d). Liquid fractions of around 0.5 are observed in transition areas between frozen and liquid particles (e.g., between 02:20 and 02:21). Regions with disagreement between the UWILD and PID phases are sometimes observed below the melting layer where UWILD shows some frozen particles (e.g., from 02:30 to 02:31). These occasional discrepancies are explained with the findings of Atlas et al. (2021) who point out that the UWILD algorithm sometimes misclassifies large liquid drops as frozen particles. Since our analysis focuses on the large end of the size spectrum, this known problem affects the comparison. Another observation is that HCR and HSRL are often able to detect hydrometeors in areas where UWILD does not detect anything (e.g. between 02:22 and 02:24). We speculate, that owing to the larger sample volume, the remote sensing instruments are more capable of detecting particles in sparsely populated regions, and are also more sensitive to the presence of very small particles, as UWILD does not classify particles with area equivalent diameters of less than 0.056 mm (Atlas et al., 2021).

To facilitate a statistical comparison between the UWILD and PID phases, liquid fractions were computed from the simplified PID classification. For the comparison with the UWILD liquid fraction, we were interested in the remote sensing observations closest to the aircraft to minimize spatial separation between the remote and in-situ data. For each second in the UWILD dataset, we collect the PID results between two seconds before and two seconds after the UWILD timestamp, and from the first six valid HCR-HSRL range gates, which correspond to ranges of ~107 to 203 m from the aircraft. This sample volume is referred to as a *PID bucket*. The PID bucket consists of 54 pixels: nine pixels along-track (i.e., in time) multiplied by six range pixels. It is important to note that the vertical offset between the UWILD data, which was collected on the aircraft, and the remote sensing measurements, can affect the comparison results (Section 4.4). A liquid fraction for the PID bucket was estimated by dividing the number of liquid pixels by the total number of non-empty pixels, provided the total number of non-empty pixels was larger than 14 (~25% of the total 54 pixels). Melting pixels in the

simplified PID bucket were equally distributed between the liquid and frozen phases. Also, the dominant (i.e., most frequently occurring) PID category for each PID bucket was recorded.

The PID liquid fraction and the UWILD liquid fraction represent different temporal and spatial domains. The UWILD bucket corresponds to 1 second of data while the PID bucket corresponds to 4.5 seconds and the PID bucket volume is therefore significantly larger than that of the UWILD bucket. The difference in volume is unavoidable because of the vertical offset. However, it can compensate for some of the effects of the offset, as explained in the following. If the aircraft is flying in a horizontally and vertically homogeneous region with particles of only frozen (e.g. 02:22:20 UTC, Figure 2d) or only liquid phase (e.g. 02:26:00, Figure 2d), the liquid fraction calculated from both the UWILD and the PID buckets will be close to 0 or 1, respectively, and the different volumes have no effect on the comparison. This was the most frequent case. The volume difference comes into play in transition areas where both frozen and liquid particles exist (02:21:10 UTC, Figure 2d). Because these transition areas are rarely vertically aligned, they will likely be observed at slightly different times in the two datasets because of the vertical offset between the measurement locations. By spreading the PID bucket in time, the likelihood of including grid points of both phases increases and the liquid fraction will therefore have more resemblance to the liquid fraction from the UWILD bucket. Therefore, we argue that the liquid fractions, although derived in very different ways, are still reasonably comparable, and the conclusions on the performance of the algorithm drawn from the following statistical analysis of the validation data is valid.

The overall Pearson correlation coefficient between the two liquid fractions in the validation data is 0.75. (P-values for this and all following correlation coefficients were less than 0.001.) However, given the sampling volume differences in the calculation of the two liquid fractions, the correlation coefficient needs to be approached with caution. We therefore conducted a heatmap comparison between the PID and UWILD liquid fractions (Figure 3) calculated for all particles (Figure 3j), and individually for the PID categories recorded as dominant for each PID bucket (see above). The heat maps show good overall agreement between the UWILD and combined PID datasets for categories with large numbers of samples. If the datasets were in perfect agreement, fractional values would align along the diagonal from the bottom left to the top right. The lower-left corner represents particles identified as frozen by both methods (liquid fraction equals zero) and the upper right corner represents particles identified as

liquid by both methods (liquid fraction equals one). Values near the upper left and bottom right corners represent disagreement in particle phase identification. Such disagreements are mostly seen in particle categories with very small sample numbers such as rain, SC rain, and melting (Figure 3a, b, and g, respectively). Both datasets favor a binary distribution of classifications as either frozen (close to zero) or liquid (close to one). The values in between, which indicate mixed conditions, are sparsely populated. (This is the reason we chose a heat map display over a scatter plot.)

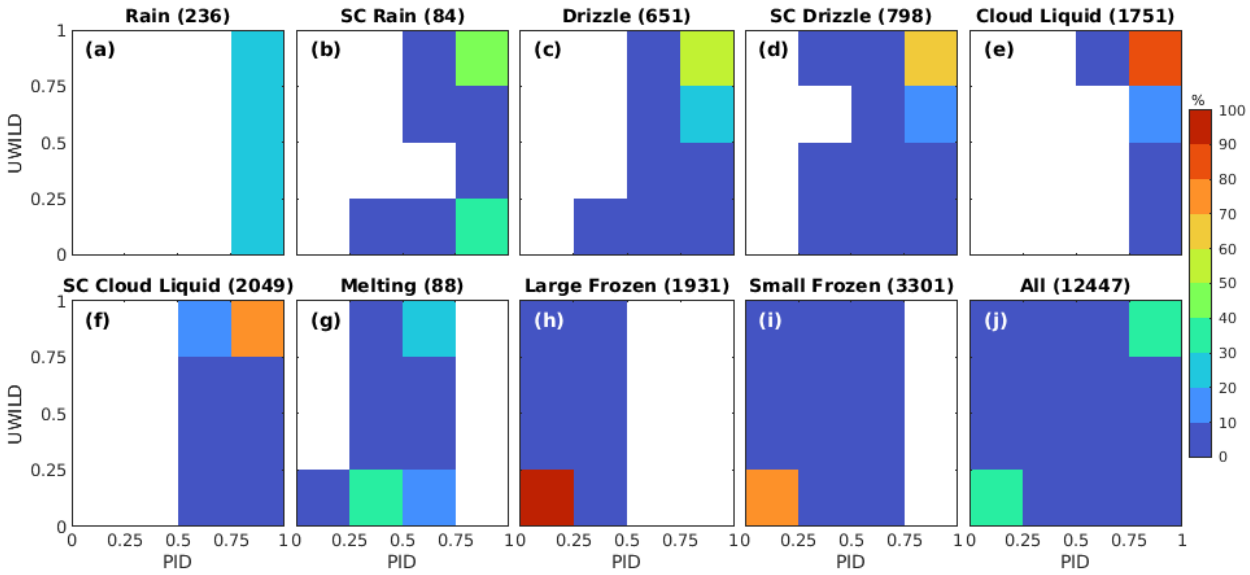

Figure 3. Heat map of PID (x-axis) vs UWILD (y-axis) liquid fractions calculated from the validation dataset. Shown are percentages of total data points (color scale). The number of points is shown in the panel titles.

About 36.0% of particles in the validation data were classified as frozen (Figure 3j) and 35.5% were classified as liquid by both algorithms. The remaining particles were evenly distributed over the other bins, none of which exceeded 10%. This even distribution of the remaining particles indicates that there is no overall systematic bias. We calculated a hit rate by adding up the percentages that lie on the aforementioned bottom-left to top-right diagonal. For all particles combined, the hit rate is 72% (Table 1).

Analyzing the particle categories individually, it is apparent that most of the SOCRATES flight tracks in the validation dataset occurred above the melting layer and less than 1,000 verification data points were collected in the rain, drizzle, and melting categories, respectively (Table 1). The SC rain category is also sparsely populated (84), reflecting the fact that

SOCRATES occurred in an environment not conducive to strong convection, which is a prerequisite for rain particles being lifted above the melting layer. The only warm particle category with a substantial number of samples (1751) is cloud liquid. For both large and small frozen particles both methods identified a large proportion of particles as frozen and the hit rates of 95% and 72% underline the good agreement between the UWILD and PID results. For the liquid categories, cloud liquid and SC cloud liquid also have high hit rates of 88% and 71% respectively. SC drizzle has a hit rate of 68%, which is lower than the hit rate of cloud liquid. Rain, SC rain, and drizzle have hit rates of 22%, 44% and 57% respectively. The low hit rates of the rain and SC rain categories are likely caused by a combination of low sample numbers and some misclassifications of large liquid particles as snow by the UWILD algorithm (Section 2.3). The melting category cannot be verified with the UWILD dataset since the latter does not identify melting particles.

Table 1. Hit rate, correlation coefficient, and number of samples for the comparison between UWILD and PID liquid fractions of the validation dataset. Numbers shown are for the HCR-HSRL combined algorithm (with sub-categories), the HCR stand-alone algorithm, regions with only LLDR observations, and regions with overlapping LDR and LLDR observations.

	Hit rate (%)	**Pearson correlation coefficient (all p<0.001)**	**Samples**
Combined all	72	0.75	12447
Combined rain	22		236
Combined SC rain	44		84
Combined drizzle	57		651
Combined SC drizzle	68		798
Combined cloud liquid	88		1751
Combined SC cloud liquid	71		2049
Combined melting			88
Combined large frozen	95		1931
Combined small frozen	72		3301
HCR stand-alone	77	0.79	11665
LLDR regions	61	0.44	8200

LDR LLDR overlap regions	77	0.82	11310

To validate the performance of the phase-defining fields from HCR (LDR) and HSRL (combination of LLDR and BACKSCAT) separately, we first applied the above-described validation method to the HCR stand-alone results. The correlation coefficient between the liquid fraction from the HCR stand-alone PID validation data and the UWILD liquid fraction is 0.79, slightly higher than the correlation coefficient of the combined PID (Table 1). The hit rate is 77%. We then applied the validation scheme to regions where LDR is not observed, but LLDR is, to validate the performance of the LLDR-BACKSCAT combination. Note that all sizes of the UWILD dataset were used for this comparison instead of just the largest ones. The resulting correlation coefficient of 0.44 is relatively low. However, the hit rate of 61% still indicates significant skill. The best comparison results are obtained in regions where all three phase-defining fields are measured: the correlation coefficient is 0.82 and the hit rate is 77% (Table 1).

It is encouraging that results from regions where not all phase-defining fields are measured still show positive skill. The results from the HCR stand-alone algorithm promise robust particle identification for field campaigns in which HSRL is not deployed. However, the excellent results from regions with all three phase-defining fields, and the expanded data regions with phase classification resulting from the addition of LLDR, highlight the benefit of deploying HCR and HSRL together. It is also worth mentioning that during the visual inspection of the PID results we rarely found non-realistic boundaries of PID categories where regions with all phase defining fields bordered regions with fewer phase defining fields. In most cases particle phase did not change at such boundaries, which again points to the skill of the phase defining fields.

4.3 Cloud liquid in regions of low DBZ

In earlier versions of the PID algorithm (not published) we did not include the post-processing step which classifies DBZ≤-30 dBZ as cloud liquid (Section 3.3). However, during our work on the PID scheme, we noticed that regions above the melting layer with very low reflectivities were mostly classified as cloud liquid in regions where LDR, LLDR, or both were observed. We analyzed the frequency of occurrence of the particle classes in regions of DBZ≤-30 dBZ (Figure 4). It is evident that the vast majority of particles are in the SC cloud liquid and cloud liquid categories (67% combined) while only 29% of particles were in the frozen categories (the remaining 4% were classified as melting). When we restricted the classification to

regions with LDR but no LLDR, the liquid percentage even increased to 97%. Based on these inferences, we assigned low reflectivity areas with the SC cloud liquid classification. The threshold of -30 dBZ was chosen empirically after conducting sensitivity studies where we varied this threshold over a certain range. At threshold values below ~-26 dBZ the liquid percentage stabilized to just below 70%. Therefore, a threshold of -30 dBZ is a conservative choice that ascertains that a possible overestimate of liquid stays below 30%.

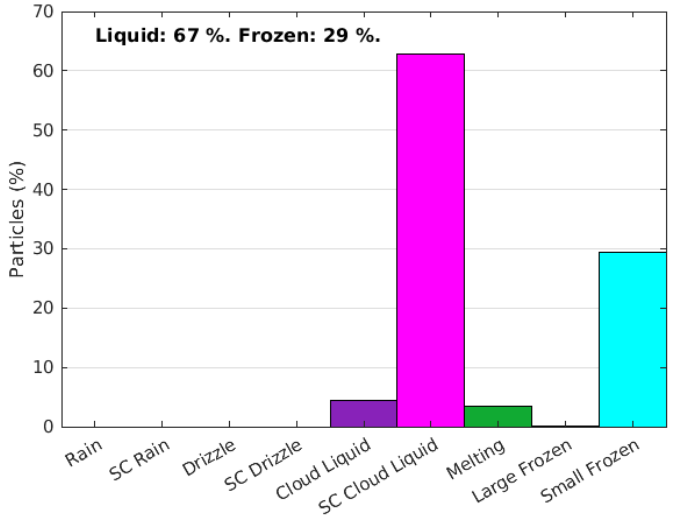

Figure 4. Particle categories of data points with DBZ≤-30 dBZ where LDR, LLDR, or both were observed.

Future studies will investigate whether the phenomenon that low reflectivities are mostly observed in liquid regions is temperature-dependent.

4.4 Caveats for the phase classification

Overall, the high correlation coefficients and hit rates from an independent dataset validate the quality of the PID results. This section presents limiting factors that may account for the discrepancies in the results, and circumstances where caution in the interpretation of the PID results is warranted.

Occasional misclassifications of liquid drops below the melting layer as frozen in the UWILD dataset (Atlas et al., 2021) is likely reflected in some of the results where PID classifies liquid but UWILD classifies frozen particles.

The most significant limiting factor to the comparison between PID and UWILD data is the spatial offset of about 100 to 200 m between the 2D-S probe and the remote sensing

observations (Section 4.1). Comparisons of phase classifications of the two datasets are likely less affected by this offset in areas of convection, where we expect more homogeneity in the vertical. In regions of stratiform clouds, which dominated in SOCRATES, the effect can be significant. It will be particularly strong in cases where the aircraft was flying at the upper or lower edge of a cloud. It has been previously observed that a liquid hull often surrounds ice-dominated clouds at their outer boundaries (de Boer et al., 2011). PID results strongly confirm this observation. If the aircraft flies at the top edge of a cloud within this liquid hull, UWILD will report a high liquid fraction, while PID from the nadir pointing instruments, which measure the ice inside the cloud, will report frozen particles.

The current version of the PID scheme does not include a mixed-phase category that could identify regions where both liquid and frozen particles co-exist within the same sample volume. The PID will therefore miss mixed-phase regions below the sampling grid resolution. It can identify mixed-phase regions if the dominant phase changes in consecutive grid points.

The classification of low reflectivity regions as cloud liquid likely somewhat overestimates the presence of liquid (Section 4.3). While we considered flagging these regions as mixed-phase we ultimately decided against this idea, to keep the PID classes simple. Considering that small liquid drops are associated with aircraft icing conditions and pose a significant risk for aviation, we decided to err on the side of overestimating liquid.

4.5 PID example

An example of the PID results for 19 January, 2018, between 4:25 and 4:30 UTC, is shown in Figure 5g. During this time, HCR and HSRL were operated in nadir pointing mode and sampled a mostly stratiform precipitating cloud. Measurements of all input fields for the PID scheme are shown in Figure 5a-f. Note that per the standard radar-based convention, downward motion in VEL is positive in nadir pointing mode but negative while zenith pointing.

The spatial variation in HCR and HSRL measurements suggests that liquid, frozen, and melting hydrometeors were present in the sampled cloud (Figure 5a-e), and this is reflected in the derived PID fields from the HCR/HSRL combined (Figure 5g) and HCR stand-alone algorithms (Figure 5h). As expected, regions with large values in the size defining fields DBZ and VEL were assigned to the large particle categories rain, SC rain, large frozen, and precipitation.

593

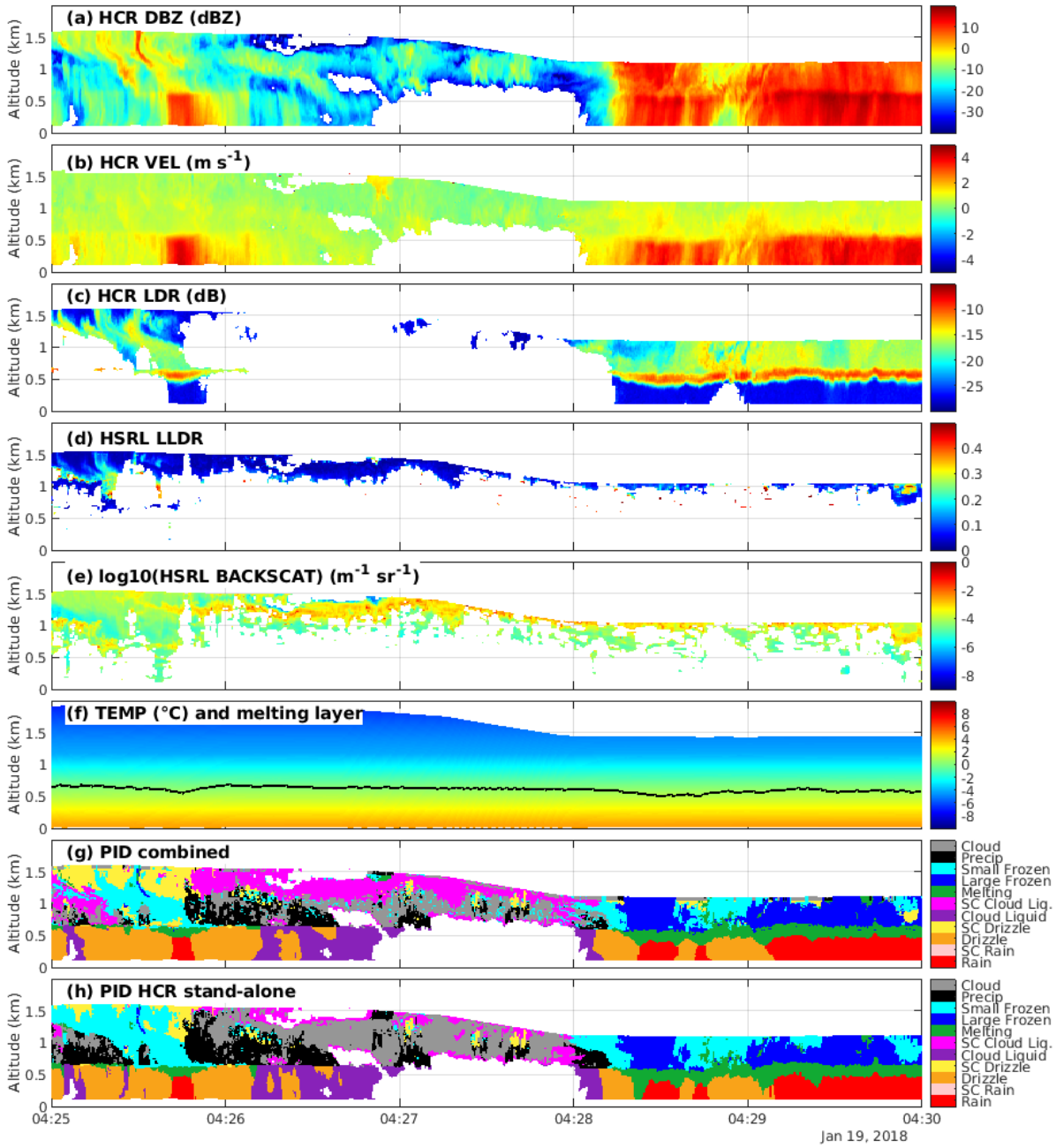

594

595 Figure 5. Input fields: (a) DBZ, (b) VEL, (c) LDR, (d) LLDR, (e) BACKSCAT, (f)
596 TEMP and melting layer. Output fields: (g) PID combined, and (h) PID HCR stand-alone.

597 A relatively narrow band around the melting layer altitude (Figure 5f) shows the highest
598 values of LDR (Figure 5c), especially in regions with large particles above and below. High
599 LDR values are associated with hydrometeor melting (Romatschke, 2021), which is consistent
600 with the melting classification in the PID field. Above the melting layer, particle phase was

assigned in regions where either LDR, LLDR, or both were measured, or DBZ≤-30 dBZ. Liquid particles were observed in regions with low LDR and LLDR, but high BACKSCAT.

Comparing the HCR/HSRL combined PID (Figure 5g) with the HCR stand-alone PID generally shows good agreement, although the combined algorithm shows enlarged drizzle regions (e.g. 04:25 to 04:26). The combined algorithm could retrieve particle phase in low reflectivity regions because of the availability of LLDR (Figure 5g) where the HCR stand-alone algorithm only provided the cloud or precipitation categories (Figure 5h). The expanded areas with phase classification demonstrate the benefit of a combined deployment of HCR and HSRL for unambiguous detection of particle phase in low reflectivity regions.

4.6 Hydrometeor size

In addition to phase discrimination, the PID scheme provides information about the sizes of the particles by classifying them as large and small for the frozen categories and rain sized, drizzle sized, and cloud droplet sized for the liquid categories. MFs were not tuned to adjust particle sizes since the categories are rather descriptive than quantitative in nature. To verify that the size distribution of the categories indeed follows the distribution implied by their names, and to assign quantitative size estimates to the qualitative category names, we used the same PID bucket that was used to calculate the PID liquid fraction and recorded the dominant (i.e. most frequent) PID category at each UWILD time step (Section 4.2). Then, for each PID category, we found the associated times in the UWILD dataset and averaged the mean size of the particles in the UWILD bucket that were recorded during the UWILD processing (Section 4.2). Since particle size was not part of the tuning process, the procedure was carried out for the whole dataset which included both the tuning and validation times. The results show that the PID categories indeed follow the expected size distribution (Figure 6).

With a mean diameter of 0.51 mm, rain has the largest average size of the liquid categories followed by SC rain with 0.44 mm. The mean drop size of rain is on the low end of the size spectrum usually attributed to rain (Houze, 2014). The small raindrop size can likely at least partially be attributed to the fact that larger particles are more likely to be partially truncated by the image buffer of the 2D-S probe (Atlas et al., 2021). Also, in an extratropical region such as the Southern Ocean it is reasonable to expect smaller raindrop sizes. Large concentrations of cloud droplets have been observed over the Southern Ocean (Huang et al., 2015; McCoy et al.,

631 2020 & 2021; Zhou et al., 2021) which may suppress the formation of large rain drops (Beard
632 and Ochs, 1993). The small number of samples in the rain and SC rain categories (Table 1) may
633 also play a role. The mean diameters of SC drizzle (0.26 mm), and drizzle (0.24 mm) are smaller
634 than those of the rain categories, and fall well within the size ranges generally associated with
635 drizzle drops (Houze, 2014).

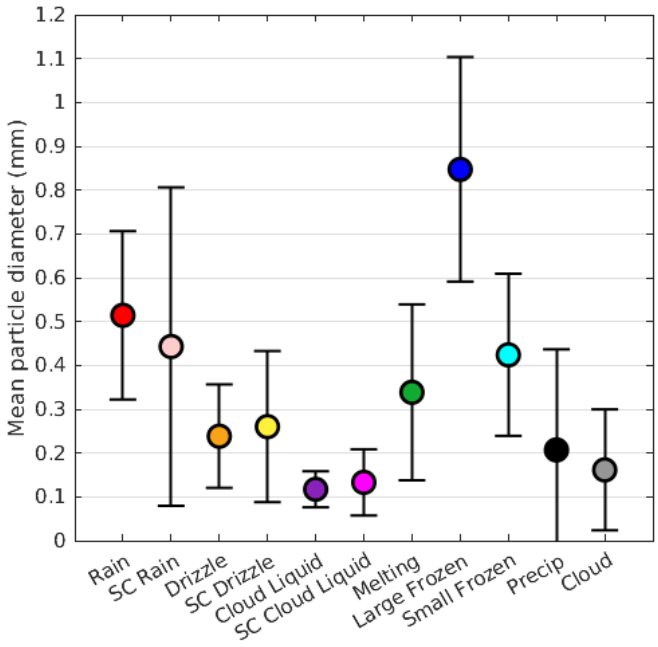

636

637 **Figure 6**. Mean particle diameter for each PID category calculated from the UWILD
638 bucket (colored dots). The black brackets show one standard deviation.

639 The cloud liquid (0.12 mm), SC cloud liquid (0.13 mm), and cloud (0.16 mm) categories
640 have the smallest diameters, as expected. However, the average diameters are larger than those
641 usually attributed to cloud droplets (Houze, 2014). The inflated size of the cloud liquid
642 categories is likely caused by the lower detection boundary of UWILD of 0.056 mm. In fact,
643 UWILD mostly does not detect any particles when PID detects cloud droplets and the actual
644 mean particle size of the cloud liquid categories is therefore likely significantly smaller.

645 Particles in the melting category, which are mostly observed close to the melting layer,
646 have an average diameter of 0.34 mm, which is between the rain and drizzle particles and smaller
647 than the frozen particles.

648 Even though large frozen particles are the largest, with an average diameter of 0.85 mm,
649 they are still significantly smaller than expected for a category that includes snowflakes.

However, the limitations of the 2D-S probe in measuring large particles likely underestimated the large frozen particle size. The actual diameters of the large frozen particles will extend to larger sizes than are reflected here. The mean diameter of the small frozen particles is reasonable at 0.42 mm with a large standard deviation. Interestingly, there is almost no overlap between the size ranges of the large and small frozen categories, with a separation boundary at 0.6 mm.

The precipitation category has an average particle diameter of 0.21 mm which may seem small at a first glance. However, we need to keep in mind that the precipitation category is only assigned in regions where neither LDR nor LLDR are observed. These regions have generally low backscattered powers and the precipitation in this category is therefore expected to be on the low end of the precipitating categories. The precipitation category also has a large standard deviation.

From Figure 6 and the previous discussion, we attribute the approximate size ranges listed in Table 2 to the PID categories.

Table 2. Approximate PID category particle diameter ranges.

PID category	Lower bound (mm)	Upper bound (mm)
Rain	0.3	
SC rain	0.1	
Drizzle	0.1	0.4
SC drizzle	0.1	0.4
Cloud liquid		0.2
SC cloud liquid		0.2
Melting	0.1	0.5
Large frozen	0.6	
Small frozen	0.2	0.6
Precipitation		0.4
Cloud		0.3

5 Conclusions

Remote sensing observations from the airborne HIAPER Cloud Radar (HCR) and High Spectral Resolution Lidar (HSRL) collected in 15 research flights during the SOCRATES field

campaign over the Southern Ocean were used for the development of a PID scheme. It discriminates between liquid and frozen cloud and precipitation particles of different sizes, and classifies them into eleven particle categories. The fuzzy logic based PID method results in smooth transitions between particle types instead of fixed borders and combines several different input fields into a robust PID classification. The mathematical steps are simple, linear, algebraic operations, hence the PID technique can be implemented for real-time applications. A trimmed-down version of the algorithm can be used for HCR data alone.

In-situ measurements collected onboard the HIAPER aircraft by a 2D-S cloud probe, which had previously been processed with machine learning methods, were used to tune the algorithm and verify the PID results. A comparison between the phases derived from the HCR and 2D-S cloud probe measurements shows over 70% agreement, which is encouraging given the comparison's limitations, such as a spatial offset between in-situ and remote measurements. The sizes of the PID particle categories derived from the 2D-S size distributions fall within the expected ranges.

Adding particle identification capabilities to HCR, and HCR and HSRL in combination, significantly increases the cloud and precipitation particle information available to the research community. The PID field adds a two-dimensional (time-range) dataset that provides vertical slices through clouds and precipitation systems, to the one-dimensional (time) cloud probe data, which are only available at the flight level. Also, the combination of the large sample volume and the sensitivity of the remote sensing instruments provides hydrometeor phase and size information in areas where cloud probe data is limited. PID is available for all past HCR and HCR/HSRL combined field campaigns and will be provided in the standard datasets of future campaigns.

The spatial distribution of both hydrometeor phase and size, derived from remote sensing observations in the PID scheme, can constrain microphysical parameterization in weather and climate models and improve the representation of cloud radiative effects. Quantification of precipitation amounts can be improved by modifying precipitation estimation techniques based on particle type.

Acknowledgments

This material is based upon work supported by the National Center for Atmospheric Research, which is a major facility sponsored by the National Science Foundation under Cooperative Agreement No. 1852977. The authors thank Michael Dixon for the creation of the HCR/HSRL combined data product and the NCAR/EOL HCR and HSRL teams for the flawless performance of the remote sensing instruments. We thank Julian Schima and Greg McFarquhar for helpful feedback on the algorithm. We thank Michael Dixon and Matthew Hayman for valuable comments on the manuscript.

Data availability statement

All input data and the resulting PID fields are available in the EOL Field Data Archive https://data.eol.ucar.edu: HCR 10 Hz data at https://doi.org/10.5065/D68914PH (NCAR/EOL HCR Team, 2022b) and HCR/HSRL 2 Hz data at https://doi.org/10.5065/D64J0CZS (NCAR/EOL HCR Team & NCAR/EOL HSRL Team, 2022a), and UWILD data at https://doi.org/10.26023/PA5W-4DRX-W50A (Atlas et al., 2021).

References

Albrecht, B., Ghate, V., Mohrmann, J., Wood, R., Zuidema, P., Bretherton, C., et al. (2019). Cloud System Evolution in the Trades—CSET. *Bulletin of the American Meteorological Society*, 100(1), 93–121. https://doi.org/10.1175/BAMS-D-17-0180.1

Atlas, R., Mohrmann, J., Finlon, J., Lu, J., Hsiao, I., Wood, R., & Diao, M. (2021). The University of Washington Ice–Liquid Discriminator (UWILD) improves single-particle phase classifications of hydrometeors within Southern Ocean clouds using machine learning. *Atmospheric Measurement Techniques*, 14(11), 7079–7101. https://doi.org/10.5194/amt-14-7079-2021

Beard, K. V., & Ochs , H. T., III (1993). Warm-Rain Initiation: An Overview of Microphysical Mechanisms. *Journal of Applied Meteorology and Climatology*, 32, 4, 608-625. https://doi.org/10.1175/1520-0450(1993)032<0608:WRIAOO>2.0.CO;2

Bjordal, J., Storelvmo, T., Alterskjær, K., & Carlsen, T. (2020). Equilibrium climate sensitivity above 5 °C plausible due to state-dependent cloud feedback. *Nat. Geosci.* 13, 718–721. https://doi-org.cuucar.idm.oclc.org/10.1038/s41561-020-00649-1

de Boer, G., Morrison, H., Shupe, M. D., & Hildner, R. (2011). Evidence of liquid dependent ice nucleation in high-latitude stratiform clouds from surface remote sensors. *Geophysical Research Letters*, 38(1). https://doi.org/10.1029/2010GL046016

Ceccaldi, M., Delanoë, J., Hogan, R. J., Pounder, N. L., Protat, A., & Pelon, J. (2013). From CloudSat-CALIPSO to EarthCare: Evolution of the DARDAR cloud classification and its comparison to airborne radar-lidar observations. *Journal of Geophysical Research: Atmospheres*, 118(14), 7962–7981. https://doi.org/10.1002/jgrd.50579

Chilson, C., Avery, K., McGovern, A., Bridge, E., Sheldon, D. and Kelly, J. (2019). Automated detection of bird roosts using NEXRAD radar data and Convolutional Neural Networks. *Remote Sens Ecol Conserv*. 5: 20-32. https://doi-org.cuucar.idm.oclc.org/10.1002/rse2.92

Dolan, B., & Rutledge, S. A. (2009). A Theory-Based Hydrometeor Identification Algorithm for X-Band Polarimetric Radars. *Journal of Atmospheric and Oceanic Technology*, 26, 10, 2071-2088. https://doi.org/10.1175/2009JTECHA1208.1

Ellis, S. M., & Vivekanandan, J. (2011). Liquid water content estimates using simultaneous S and Ka band radar measurements. *Radio Science*, 46(2). https://doi.org/10.1029/2010RS004361

Ellis, S. M., Tsai, P., Burghart, C., Romatschke, U., Dixon, M., Vivekanandan, J., et al. (2019). Use of the Earth's Surface as a Reference to Correct Airborne Nadir-Looking Radar Radial Velocity Measurements for Platform Motion. *Journal of Atmospheric and Oceanic Technology*, 36(7), 1343–1360. https://doi.org/10.1175/JTECH-D-19-0019.1

European Centre for Medium-Range Weather Forecasts. (2018). ERA5 Reanalysis (0.25 Degree Latitude-Longitude Grid), Accessed 07 May 2018. https://doi.org/10.5065/BH6N-5N20

Fuchs-Stone, Ž., Raymond, D. J., & Sentić, S. (2020). OTREC2019: Convection Over the East Pacific and Southwest Caribbean. *Geophysical Research Letters*, 47(11), e2020GL087564. https://doi.org/10.1029/2020GL087564

Garcia-Benadi A., Bech J., Gonzalez S., Udina M., Codina B., Georgis J-F. (2020). Precipitation Type Classification of Micro Rain Radar Data Using an Improved Doppler Spectral Processing Methodology. *Remote Sensing*, 12(24):4113. https://doi.org/10.3390/rs12244113

753 Houze, R. A. (2014). *Cloud Dynamics*. Academic Press.

754 Huang, Y., Protat, A., Siems, S. T., & Manton, M. J. (2015). A-Train Observations of
755 Maritime Midlatitude Storm-Track Cloud Systems: Comparing the Southern Ocean against the
756 North Atlantic. *Journal of Climate*, 28, 5, 1920-1939. https://doi.org/10.1175/JCLI-D-14-
757 00169.1

758 Illingworth, A. J., Hogan, R. J., O'Connor, E.J., Bouniol, D., Brooks, M. E., Delanoé, J.,
759 Donovan, D. P., Eastment, J. D., Gaussiat, N., Goddard, J. W. F., Haeffelin, M., Baltink, H. K.,
760 Krasnov, O. A., Pelon, J., Piriou, J.-M., Protat, A., Russchenberg, H. W. J., Seifert, A.,
761 Tompkins, A. M., van Zadelhoff, G.-J., Vinit, F., Willén, U., Wilson, D. R., & Wrench, C. L.
762 (2007). Cloudnet. *Bulletin of the American Meteorological Society*, 88, 6, 883-898.
763 https://doi.org/10.1175/BAMS-88-6-883

764 Jatau, P., Melnikov, V., & Yu, T. (2021). A Machine Learning Approach for Classifying
765 Bird and Insect Radar Echoes with S-Band Polarimetric Weather Radar. *Journal of Atmospheric*
766 *and Oceanic Technology*, 38, 10, 1797-1812. https://doi-
767 org.cuucar.idm.oclc.org/10.1175/JTECH-D-20-0180.1

768 Kalesse-Los, H., Schimmel, W., Luke, E., and Seifert, P. (2022). Evaluating cloud liquid
769 detection against Cloudnet using cloud radar Doppler spectra in a pre-trained artificial neural
770 network. *Atmos. Meas. Tech*., 15, 279–295. https://doi.org/10.5194/amt-15-279-2022

771 Khain, A., Pokrovsky, A., Pinsky, M., Seifert, A., & Phillips, V. (2004). Simulation of
772 Effects of Atmospheric Aerosols on Deep Turbulent Convective Clouds Using a Spectral
773 Microphysics Mixed-Phase Cumulus Cloud Model. Part I: Model Description and Possible
774 Applications. *Journal of the Atmospheric Sciences* 61, 24, 2963-2982.
775 https://doi.org/10.1175/JAS-3350.1

776 Khain, A., Lynn, B., & Dudhia, J. (2010). Aerosol Effects on Intensity of Landfalling
777 Hurricanes as Seen from Simulations with the WRF Model with Spectral Bin Microphysics.
778 *Journal of the Atmospheric Sciences* 67, 2, 365-384. https://doi.org/10.1175/2009JAS3210.1

779 Kikuchi, M., Okamoto, H., Sato, K., Suzuki, K., Cesana, G., Hagihara, Y., et al. (2017).
780 Development of Algorithm for Discriminating Hydrometeor Particle Types With a Synergistic

781 Use of CloudSat and CALIPSO. *Journal of Geophysical Research: Atmospheres*, 122(20),
782 11,022-11,044. https://doi.org/10.1002/2017JD027113

783 Komurcu, M., Storelvmo, T., Tan, I., Lohmann, U., Yun, Y., Penner, J. E., Wang, Y.,
784 Liu, X., & Takemura, T. (2014). Intercomparison of the cloud water phase among global climate
785 models, *J. Geophys. Res. Atmos*., 119, 3372– 3400, https://doi.org/10.1002/2013JD021119.

786 Korolev, A., & Isaac, G. (2003). Phase transformation of mixed-phase clouds. Quarterly
787 *Journal of the Royal Meteorological Society*, 129(587), 19–38. https://doi.org/10.1256/qj.01.203

788 Lawson, R. P., O'Connor, D., Zmarzly, P., Weaver, K., Baker, B., Mo, Q., & Jonsson, H.
789 (2006). The 2D-S (Stereo) Probe: Design and Preliminary Tests of a New Airborne, High-Speed,
790 High-Resolution Particle Imaging Probe. *Journal of Atmospheric and Oceanic Technology*,
791 23(11), 1462–1477. https://doi.org/10.1175/JTECH1927.1

792 Lim, S., Chandrasekar, V., & Bringi, V. N. (2005). Hydrometeor classification system
793 using dual-polarization radar measurements: model improvements and in situ verification. *IEEE*
794 *Transactions on Geoscience and Remote Sensing*, 43, 4, 792-801.
795 https://doi.org/10.1109/TGRS.2004.843077

796 Lin, Y., & Colle, B. A. (2011). A New Bulk Microphysical Scheme That Includes
797 Riming Intensity and Temperature-Dependent Ice Characteristics. *Monthly Weather Review* 139,
798 3, 1013-1035. https://doi.org/10.1175/2010MWR3293.1

799 Liu, H., & Chandrasekar, V. (2000). Classification of Hydrometeors Based on
800 Polarimetric Radar Measurements: Development of Fuzzy Logic and Neuro-Fuzzy Systems, and
801 In Situ Verification. *Journal of Atmospheric and Oceanic Technology*, 17, 2, 140-164.
802 https://doi.org/10.1175/1520-0426(2000)017<0140:COHBOP>2.0.CO;2

803 Luke, E. P., Kollias, P., & Shupe, M. D. (2010). Detection of supercooled liquid in
804 mixed-phase clouds using radar Doppler spectra, *J. Geophys. Res.*, 115, D19201.
805 https://doi.org/10.1029/2009JD012884

806 McCarthy, N. F., Guyot, A., Protat, A., Dowdy, A. J., & McGowan, H. (2020). Tracking
807 pyrometeors with meteorological radar using unsupervised machine learning. *Geophysical*
808 *Research Letters*, 47. https://doi-org.cuucar.idm.oclc.org/10.1029/2019GL084305

McCoy, D. T., Hartmann, D. L., & Grosvenor, D. P. (2014). Observed Southern Ocean Cloud Properties and Shortwave Reflection. Part I: Calculation of SW Flux from Observed Cloud Properties. *Journal of Climate* 27, 23, 8836-8857. https://doi.org/10.1175/JCLI-D-14-00287.1

McCoy, I. L., McCoy, D. T., Wood, R., Regayre, L., Watson-Parris, D., Grosvenor, D. P., Mulcahy, J. P., Hu, Y., Bender, F. A. M., Field, P. R., Carslaw, K. S., & Gordon, H. (2020). The hemispheric contrast in cloud microphysical properties constrains aerosol forcing. *Proceedings of the National Academy of Sciences of the United States of America*, 117(32), 18998– 19006. https://doi-org.cuucar.idm.oclc.org/10.1073/pnas.1922502117

McCoy, I. L., Bretherton, C. S., Wood, R., Twohy, C. H., Gettelman, A., Bardeen, C. G., & Toohey, D. W. (2021). Influences of recent particle formation on Southern Ocean aerosol variability and low cloud properties. *Journal of Geophysical Research: Atmospheres*, 126, e2020JD033529. https://doi-org.cuucar.idm.oclc.org/10.1029/2020JD033529

McFarquhar, G. M., Bretherton, C., Marchand, R., Protat, A., DeMott, P. J., Alexander, S. P., et al. (2020). Observations of clouds, aerosols, precipitation, and surface radiation over the Southern Ocean: An overview of CAPRICORN, MARCUS, MICRE and SOCRATES. *Bulletin of the American Meteorological Society*, 1(aop), 1–92. https://doi.org/10.1175/BAMS-D-20-0132.1

Mohrmann, J., Finlon, J., Atlas, R., Lu, J., Hsiao, I., & Wood, R. (2021). University of Washington Ice-Liquid Discriminator single particle phase classifications and 1 Hz particle size distributions/heterogeneity estimate. Version 1.0, Accessed 01 Jul 2021. https://doi.org/10.26023/PA5W-4DRX-W50A

Morrison, H., Thompson, G., & Tatarskii, V. (2009). Impact of Cloud Microphysics on the Development of Trailing Stratiform Precipitation in a Simulated Squall Line: Comparison of One- and Two-Moment Schemes. *Monthly Weather Review* 137, 3, 991-1007. https://doi.org/10.1175/2008MWR2556.1

Morrison, H., van Lier-Walqui, M., Fridlind, A. M., Grabowski, W. W., Harrington, J. Y., Hoose, C., et al. (2020). Confronting the Challenge of Modeling Cloud and Precipitation

Microphysics. *Journal of Advances in Modeling Earth Systems*, 12(8), e2019MS001689. https://doi.org/10.1029/2019MS001689

NCAR/EOL HCR Team (2022a). CSET: NCAR HCR radar moments data. Version 3.0, Accessed 19 Jan 2022. https://doi.org/10.5065/D6CJ8BV7

NCAR/EOL HCR Team. (2022b). SOCRATES: NCAR HCR radar moments data. Version 3.0, Accessed 19 Jan 2022. https://doi.org/10.5065/D68914PH

NCAR/EOL HCR Team. (2022c). OTREC: NCAR HCR radar moments data. Version 3.0, Accessed 19 Jan 2022. https://doi.org/10.26023/V9DJ-7T9J-PE0S

NCAR/EOL HCR Team. (2022d). SPICULE: NCAR HCR radar moments data. Version 1.1, Accessed 19 Jan 2022. https://doi.org/10.26023/PGGK-MC4T-K70F

NCAR/EOL HCR Team & NCAR/EOL HSRL Team. (2022a). CSET: NCAR HCR radar and HSRL lidar moments data. Version 3.0, Accessed 19 Jan 2022. https://doi.org/10.26023/NXR4-FTPY-J04

NCAR/EOL HCR Team & NCAR/EOL HSRL Team. (2022b). SOCRATES: NCAR HCR radar and HSRL lidar moments data. Version 3.0, Accessed 19 Jan 2022. https://doi.org/10.5065/D64J0CZS

Park, H. S., Ryzhkov, A. V., Zrnić, D. S., and Kim, K. (2009). The Hydrometeor Classification Algorithm for the Polarimetric WSR-88D: Description and Application to an MCS, *Weather and Forecasting* 24, 3, 730-748. https://doi.org/10.1175/2008WAF2222205.1

Paukert, M., Fan, J., Rasch, P. J., Morrison, H., Milbrandt, J. A., Shpund, J., & Khain, A. (2019). Three-Moment Representation of Rain in a Bulk Microphysics Model. *Journal of Advances in Modeling Earth Systems*, 11(1), 257–277. https://doi.org/10.1029/2018MS001512

Rauber, R. M., Ellis, S. M., Vivekanandan, J., Stith, J., Lee, W.-C., McFarquhar, G. M., et al. (2017). Finescale Structure of a Snowstorm over the Northeastern United States: A First Look at High-Resolution HIAPER Cloud Radar Observations. *Bulletin of the American Meteorological Society*, 98(2), 253–269. https://doi.org/10.1175/BAMS-D-15-00180.1

Razenkov, I. A., Eloranta, E. W., Hedrick, J. P., & Garcia, J. P. (2008). The Design and Construction of an Airborne High Spectral Resolution Lidar (p. 4). Presented at the 24th International Laser Radar Conference.

Roberto, N., Baldini, L., Adirosi, E., Facheris, L., Cuccoli, F., Lupidi, A., Garzelli, A. (2017). A Support Vector Machine Hydrometeor Classification Algorithm for Dual-Polarization Radar. *Atmosphere*, 8(8):134. https://doi.org/10.3390/atmos8080134

Romatschke, U. (2021). Melting Layer Detection and Observation with the NCAR Airborne W-Band Radar. *Remote Sensing*, 13(9), 1660. https://doi.org/10.3390/rs13091660

Romatschke, U., & Dixon, M. (2022). Vertically Resolved Convective/Stratiform Echo Type Identification and Convectivity Retrieval for Vertically Pointing Radars. *EarthArXiv*. https://doi.org/10.31223/X54S77

Romatschke, U., Dixon, M., Tsai, P., Loew, E., Vivekanandan, J., Emmett, J., & Rilling, R. (2021). The NCAR Airborne 94-GHz Cloud Radar: Calibration and Data Processing. *Data*, 6(6), 66. https://doi.org/10.3390/data6060066

Shupe, M. D. (2007). A ground-based multisensor cloud phase classifier. *Geophysical Research Letters*, 34(22). https://doi.org/10.1029/2007GL031008

Sokol Z., Minářová J., Fišer O. (2020). Hydrometeor Distribution and Linear Depolarization Ratio in Thunderstorms. *Remote Sensing*, 12(13):2144. https://doi.org/10.3390/rs12132144

Sun, Z. & Shine, K. P. (1994). Studies of the radiative properties of ice and mixed-phase clouds. *Q.J.R. Meteorol. Soc*., 120: 111-137. https://doi.org/10.1002/qj.49712051508

Tan, I., Storelvmo, T., & Zelinka, M. D. (2016). Observational constraints on mixed-phase clouds imply higher climate sensitivity, *Science*, 352, 224–227, https://doi.org/10.1126/science.aad5300

Tao, W.-K. & Simpson, J., (1993). Goddard Cumulus Ensemble Model. Part I: Model Description. *Terr. Atmos. Ocean. Sci*., 4, 35-75. https://doi.org/10.3319/TAO.1993.4.1.35(A)

Thompson, G., Field, P. R., Rasmussen, R. M., & Hall, W. D. (2008). Explicit Forecasts of Winter Precipitation Using an Improved Bulk Microphysics Scheme. Part II: Implementation

of a New Snow Parameterization. *Monthly Weather Review* 136, 12, 5095-5115. https://doi.org/10.1175/2008MWR2387.1

Vivekanandan, J., Zrnic, D. S., Ellis, S. M., Oye, R., Ryzhkov, A. V., & Straka, J. (1999). Cloud Microphysics Retrieval Using S-Band Dual-Polarization Radar Measurements. *Bulletin of the American Meteorological Society*, 80(3), 381–388. https://doi.org/10.1175/1520-0477(1999)080<0381:CMRUSB>2.0.CO;2

Vivekanandan, Jothiram, Ellis, S., Tsai, P., Loew, E., Lee, W.-C., Emmett, J., et al. (2015). A wing pod-based millimeter wavelength airborne cloud radar. *Geoscientific Instrumentation, Methods and Data Systems*, 4(2), 161–176. https://doi.org/10.5194/gi-4-161-2015

Vivekanandan, Jothiram, Ghate, V. P., Jensen, J. B., Ellis, S. M., & Schwartz, M. C. (2020). A Technique for Estimating Liquid Droplet Diameter and Liquid Water Content in Stratocumulus Clouds Using Radar and Lidar Measurements. *Journal of Atmospheric and Oceanic Technology*, 37(11), 2145–2161. https://doi.org/10.1175/JTECH-D-19-0092.1

Vogl, T., Maahn, M., Kneifel, S., Schimmel, W., Moisseev, D., & Kalesse-Los, H.: Using artificial neural networks to predict riming from Doppler cloud radar observations. *Atmos. Meas. Tech.*, 15, 365–381. https://doi.org/10.5194/amt-15-365-2022, 2022

Wallace, J. M. & Hobbs, P. V. (2006). *Atmospheric Science*, Academic Press.

Wood, R. (2012). Stratocumulus Clouds. *Monthly Weather Review*, 140(8), 2373–2423. https://doi.org/10.1175/MWR-D-11-00121.1

Zelinka, M. D., Myers, T. A., McCoy, D. T., Po-Chedley, S., Caldwell, P. M., Ceppi, P., Klein, S. A., & Taylor, K. E. (2020). Causes of higher climate sensitivity in CMIP6 models. *Geophysical Research Letters*, 47, e2019GL085782. https://doi.org/10.1029/2019GL085782

Zhang, G. (2019). *Weather Radar Polarimetry*. CRC Press.

Zhou, X., Atlas, R., McCoy, I. L., Bretherton, C. S., Bardeen, C., Gettelman, A., Lin, P., Ming, Y. (2021). Evaluation of cloud and precipitation simulations in CAM6 and AM4 using observations over the Southern Ocean. *Earth and Space Science*, 8, e2020EA001241. https://doi.org/10.1029/2020EA001241

Zrnić, D. S., Ryzhkov, A., Straka, J., Liu, Y., & Vivekanandan, J. (2001). Testing a Procedure for Automatic Classification of Hydrometeor Types. *Journal of Atmospheric and Oceanic Technology*, 18, 6, 892-913. https://doi.org/10.1175/1520-0426(2001)018<0892:TAPFAC>2.0.CO;2